Available online at www.sciencedirect.com
ScienceDirect
Journal of Solid State Chemistry 181 (2008) 1227–1235
JOURNAL OF SOLID STATE CHEMISTRY
www.elsevier.com/locate/jssc

Effect of heat treatment on pore structure in nano-crystalline NiO: A small angle neutron scattering study

J. Bahadur[a,*], D. Sen[a], S. Mazumder[a], S. Ramanathan[b]

[a]Solid State Physics Division, Bhabha Atomic Research Centre, Mumbai 400085, India
[b]Materials Science Division, Bhabha Atomic Research Centre, Mumbai 400085, India

Received 30 October 2007; received in revised form 28 January 2008; accepted 30 January 2008
Available online 4 March 2008

Abstract

Nano-crystalline nickel oxide powder was synthesized by a precipitation route. Powder samples were heat treated at 300, 600 and 900 °C, and pore structure evolution was followed by small angle neutron scattering (SANS) technique. SANS measurements were carried out also on pelleted samples in order to study the modifications of pore morphology due to heat treatment. SANS data reveal scattering from pores at two different length scales. The pore structure at various heat treatment temperatures does not follow any scaling behavior.

Keywords: SANS; Porous materials; Nano-ceramics; NiO

1. Introduction

Nano-materials are at the leading edge of rapidly developing field of Nanotechnology [1–4]. A reduction in particle size to nanometer scale results in various special and interesting properties compared to their bulk properties. It is worthy to mention that a major drawback of the most of the coarse grained ceramics is their brittleness. It is found that ceramics with ultra fine microstructures are more ductile and have lower sintering temperatures than their coarse-grained counterparts [5,6]. Sintering studies have been done in recent past to observe microstructure modifications. Since sintering kinetics leads to coarsening of grains particularly in final stage of sintering, different methods have been tried to obtain full dense ceramics with nano-size grains [7,8].

Ultra-fine NiO nano-ceramic particles with a uniform size and well dispersion characteristics are strongly desirable for many applications, e.g. synthesis of composite materials, magnetic, electro chromic, heterogeneous catalytic materials, etc. In addition, important applications of NiO include preparation of cathode materials of alkaline batteries, anti-ferromagnetic layers, and p-type transparent conducting films [9]. Nano-structured nickel (II) oxide is a p-type semiconductor metal oxide having a stable wide band gap. Also it can be used as a transparent p-type semiconductor layer [10]. Furthermore, it exhibits anodic electrochromism and is utilized for applications in smart windows, electrochemical super-capacitors [11,12], and dye-sensitized photo cathodes [13]. However, the functional properties of NiO vis-à-vis its applicability significantly depend on pore morphology, pore matrix-interface, and also porosity. For example, in catalytic applications the available specific surface area should be as high as possible while for the application as a cathode material, a dense material is desirable. Initial virgin powder posses large surface area relative to its volume. This surface area/surface energy provides the driving force for sintering, i.e., reduction of free surface energy resulting from the high surface area of particles [14]. Pore-size distribution and pore connectivity of particles evolve with heat treatment temperature and time. Microscopically, the sintering of crystalline solids is a result of both surface motion and grain boundary motion to minimize the total sum of surface energy and grain boundary energy.

*Corresponding author.
E-mail address: jbahadur@barc.gov.in (J. Bahadur).

0022-4596/$ - see front matter © 2008 Elsevier Inc. All rights reserved.
doi:10.1016/j.jssc.2008.01.050

Small angle neutron scattering (SANS) has been found to be a fruitful non-destructive technique to study the mesoscopic structures in porous materials [15–19]. SANS probes density fluctuations in mesoscopic length scale. Compared to other complementary techniques like mercury porosimetry, BET, etc., to study the pore structure in a porous material, SANS possess some special advantages, in particular, probing closed pores in addition to open pores. In the present study, the effects of heat treatment on pore morphology in NiO nano-ceramic have been investigated using SANS.

2. Experiments

2.1. Sample preparation

Chemical preparation of NiO nano-particles is composed of two stages: the formation of nickel hydroxide precursor precipitate and subsequent transformation to NiO by thermal treatment. Nickel hydroxide precursor, prepared by slow drop wise addition of 0.1 M sodium hydroxide (NaOH) to 0.1 M nickel nitrate $Ni(NO_3)_2$, solution was kept vigorously stirred until the pH becomes 7. Precipitate was filtered and washed repeatedly with distilled water for three times and final washing is carried out by using alcohol. Wet cake obtained after filtration was oven dried for 70 °C overnight. The oven-dried cake was heated at 300 °C for 1 h to form nano-crystalline NiO. Powder thus formed was ground in a planetary mill. Powder obtained by this method is low-density, inhomogeneous and porous, and generally lacking in physical integrity.

2.2. Powder characterization

Agglomerate size distribution of the virgin powder has been estimated using light scattering (LS) and is depicted in Fig. 1. Phase purity of the initial powder was characterized by X-ray diffraction (XRD) and is shown in Fig. 3. Morphology of the virgin powder was examined by scanning electron microscope (SEM) (Fig. 2). The initial powder sample was also heat-treated at 600 and 900 °C. Compacts of the powder were formed by uniaxial pressure at 150 MPa.

2.3. SANS experiment

SANS experiments have been performed using a double crystal based medium resolution SANS (MSANS) instrument at Guide Tube Laboratory of the Dhruva rector at Trombay, India [20]. The instrument consists of a non-dispersive (1, −1) setting of 1 1 1 reflections from a pair of single crystals with specimen between them. Scattered intensities have been recorded as a function of modulus of wave vector transfer $|q|$ [$=4\pi\sin(\theta)/\lambda$, where 2θ is the scattering angle and λ ($=0.312$ nm) is incident neutron wavelength for present experiment]. The specimens under

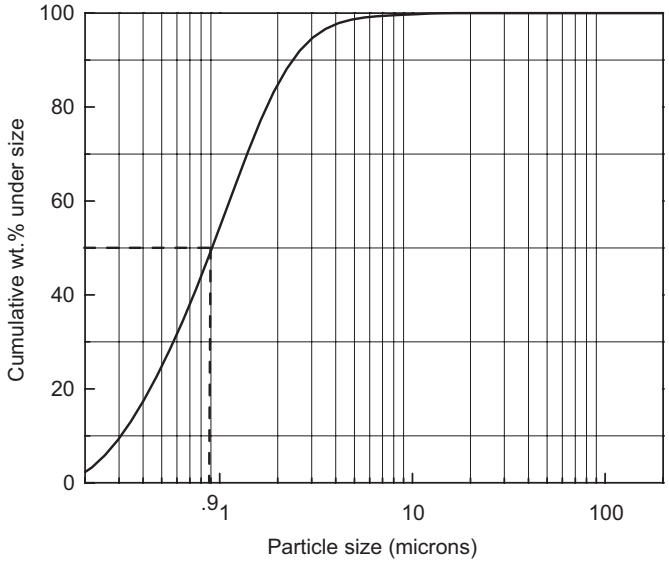

Fig. 1. Cumulative agglomerate particle size distribution of initial powder by light scattering.

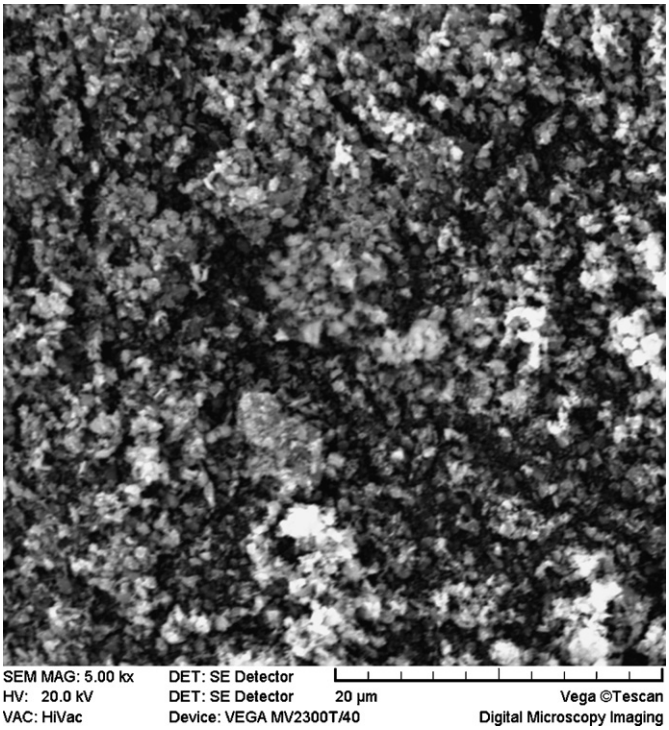

Fig. 2. SEM micrograph of the initial powder.

SANS investigations were placed on the sample holder with circular slit of ~1.5 cm diameter. SANS profiles of the specimens recorded by the instrument were corrected for smearing effect using the method given in literatures [20–23] before analysis of the data. SANS measurements have been done for 300, 600, and 900 °C heat-treated powder (Pd-300, Pd-600, and Pd-900) respectively. SANS profile for these samples are depicted in Fig. 4.

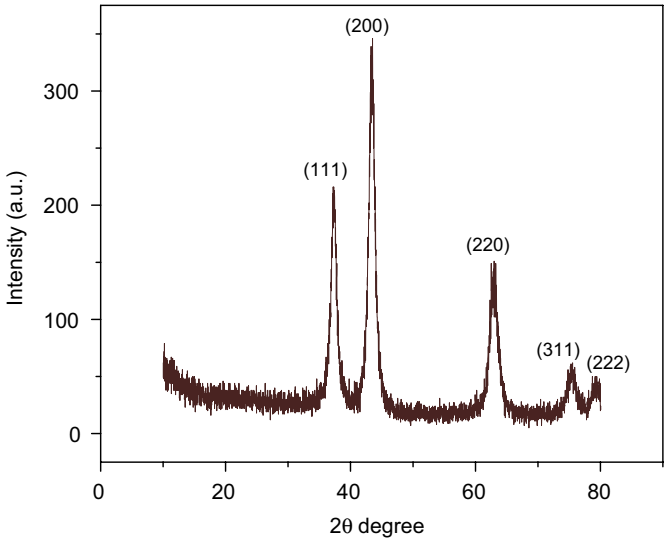

Fig. 3. XRD pattern of the initial NiO powder.

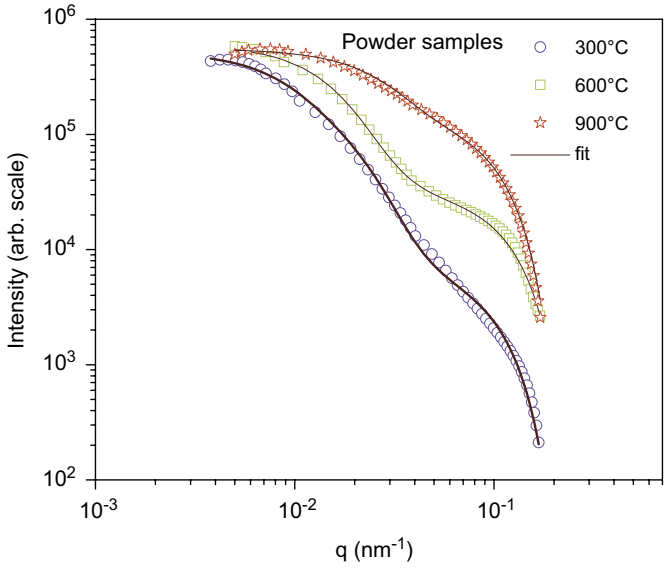

Fig. 4. Experimental SANS profiles are depicted. Solid line depicts fit of the model to data at three different heat treatment temperatures.

SANS measurements have also been done on pellets (Pl-300, Pl-600, and Pl-900), which were obtained by compaction of the powder by applying pressure in between 150 and 170 MPa. Thicknesses of the samples for SANS experiment were kept nearly 1 mm (see Appendix A) to reduce multiple scattering effects.

3. Data analysis and discussions

The median agglomerate size is of the initial powder was observed from LS is 0.9 μm. SEM micrograph also shows agglomerate nature of the initial powder. Average agglomerate size observed from SEM picture lies in the range of the size obtained by LS. Phase purity was observed by XRD. All diffraction peaks can be indexed to the pure NiO crystalline phase (space group: $Fm3m$). Crystallite size diameter (D) has been calculated by Scherrer formula:

$$D = 0.9\frac{\lambda}{\beta\cos\theta}, \tag{1}$$

where β-FWHM (full-width at half-maximum, or half-width) is in radians and θ is the position of the maximum of diffraction peak.

Crystallite size of initial powder has been found to be 9 nm.

SANS arises from the fluctuations of scattering length density in a specimen and hence SANS profile contains the information about the size/size distribution, shape, etc. of the scattering density inhomogeneities in the material (e.g. pores in a porous medium). Thus, analysis of SANS data gives information about the size/size distribution, shape, etc. of the pores in a porous medium [24–28].

It is discernible from Fig. 4 that the SANS profiles within the experimental q range can be subdivided into two regions. The first part is approximately below $q\sim0.045\,\mathrm{nm}^{-1}$ and the other is above $q\sim0.045\,\mathrm{nm}^{-1}$ and the nature of the two regions gets modified with heat treatment. This feature of the SANS data indicates the presence of inhomogenities at two length scale in the system. As expected similar trend but in different magnitudes also exists for the pelleted samples. From the SEM micrograph, it is evident that the powder grains are significantly polydisperse in nature and there exists some kind of agglomeration of the basic crystalline particles, which are of the order of 9 nm. However, both LS and SEM indicate agglomerated grains, with a length scale of nearly 1 μm. As evident from the SEM, there exists multi-levels of agglomeration in powders; possibility of pore structure in different length scale cannot be ruled out. In fact, it will be seen later on that the present SANS data within the experimental q range indicate the presence of pore structures at two widely separated length scales. So, present SANS data should be analyzed without invoking any fractal structure model. For, simplicity and also to reduce the number of unknown parameters during the SANS analysis the shape of the pores has been considered as spherical. In fact, this approximation is quite valid for the present case, as no structural feature with high aspect ratio is observed from SEM picture.

The scattering intensity from an ensemble of monodisperse spherical pores is given by

$$I(q) \propto \frac{\mathrm{d}\Sigma(\Omega)}{\mathrm{d}\Omega} = \frac{N}{V}(\rho_{\mathrm{matrix}} - \rho_{\mathrm{pores}})^2 V_{\mathrm{p}}^2 P(q), \tag{2}$$

where $\mathrm{d}\Sigma/\mathrm{d}\Omega$ is called the macroscopic differential scattering cross-section; N is the total number of pores in the sample volume V; ρ represents the scattering length density; and $(\rho_{\mathrm{matrix}}-\rho_{\mathrm{pore}})^2$ is called contrast factor between matrix and pore. V_{p} is the volume of a pore.

Since $\rho_{\mathrm{pore}} = 0$, the contrast factor between matrix and pores will be ρ^2_{matrix}. Here $P(q)$ is called the form factor and

in case of spherical pores, is given by

$$P(q) = |F(q)|^2 = 9\left[\frac{\sin(qR) - qR\cos(qR)}{(qR)^3}\right]^2. \quad (3)$$

The above equation translates for an ensemble of polydisperse system into the following equation

$$I(q) = C\int D(R)V^2(R)P(q,R)\,dR, \quad (4)$$

where $D(R)$ is size distribution, i.e., $D(R)\,dR$ represents the probability of having pores with radius between R and $R+dR$. $V(R)$ is the volume ($[4\pi/3]R^3$) of a pore of radius R. Integration limits have been taken as $R_{min}(\sim\pi/q_{max})$ and $R_{max}(\sim\pi/q_{min})$, where q_{max} and q_{min} are the instrument resolution. C is a scale factor, which is independent of q but depends on the scattering contrast between the matrix and the pores. For the present work, $D(R)$ has been taken as Weibull distribution [29], i.e.,

$$D(r,a,b) = \left(\frac{b}{a}\right)\left(\frac{r}{a}\right)^{b-1}\exp\left[-\left(\frac{r}{a}\right)^b\right], \quad (5)$$

where a and b are two parameters of the distribution, a determines the scale of the distribution, and b represents the shape of the distribution. This distribution has a special feature that it can be skewed in both sides depending on the values of a and b.

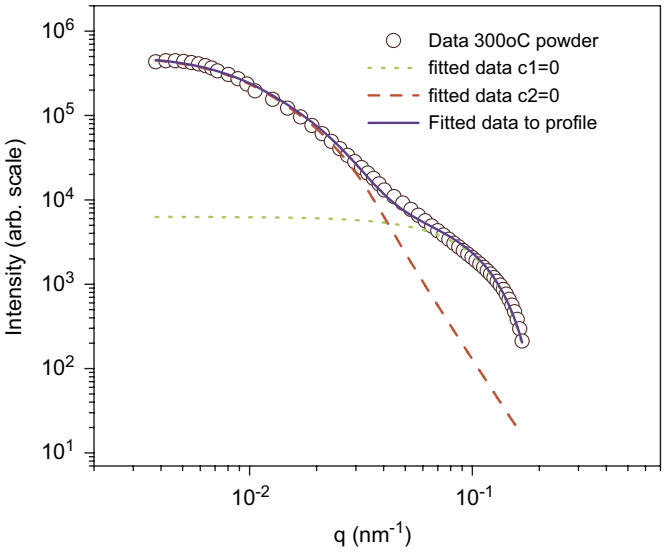

Fig. 5. Details of the model fitting to experimental data for 300 °C powder sample with two-length scale pore size distribution.

Eq. (4) has been tried to be fitted with the SANS profiles. However, it has been found that only one distribution could not explain the whole SANS profile, but it needs at least two distributions to describe well the SANS profiles in the whole q range. This is explained in Fig. 5. It is clear from Fig. 5 that the combination of the two dotted curves which originates from two distribution of pores, can give a reasonable good fit to the experimental SANS data (as shown by the solid line in Fig. 5). Hence, to incorporate the effect of two types of pore structures (type-1 for the larger pores and type-2 for the smaller pores), the SANS data have been analyzed in the light of the following extended model:

$$I(q) = C_1\int P(q,R_1)V_P^2 D_{larger}(R_1)\,dR_1 + C_2\int P(q,R_2)V_P^2 D_{smaller}(R_2)\,dR_2. \quad (6)$$

At this point it is worthy to mention that no inter-pore positional correlation has been considered here in the analysis in order to avoid too many parameters in the fitting procedure, which may sometimes end up into a situation of some non-physical parameters during fitting. The important parameters obtained from the fitting are tabulated in Table 1. Estimated larger pore size distribution (type-1 pores), for samples pd-300, pd-600, and pd-900, respectively, estimated from the analysis are depicted in Fig. 6. It is evident from the figure that the distribution becomes somewhat less polydisperse with increase in heat treatment temperature. Further, the average value of the distribution shifts towards lower radius side. The high-end tail part of the distribution is significantly modified after heat treatment. These observations can be explained on the basis of the morphological modification during heat treatment. During the initial stage of heat treatment, neck begins to form between the two agglomerated particles. Neck formation is driven by the energy gradient resulting from the difference in curvatures of the particle and that of the neck. In this process surface diffusion is the primary transport mechanism, and subsequently the adjacent necks begin to impinge upon each other. Densification and grain growth start in this process. Bulk transport mechanisms, such as grain boundary diffusion and volume diffusion, dominate the heat treatment process during the later stage. This leads to the shrinkage of the intra-agglomerate pores, and this process also involves the reduction in the polydispersity of the pore size. The type-2 (smaller length scale) pore size distributions for the samples pd-300,

Table 1
Parameters of the pore size distributions for powder samples

Sample (°C)	$\langle r_{larger}\rangle$ (nm)	$[\langle r^2_{larger}\rangle - \langle r_{larger}\rangle^2]^{0.5}$ (nm)	$\langle r_{smaller}\rangle$ (nm)	$[\langle r^2_{smaller}\rangle - \langle r_{smaller}\rangle^2]^{0.5}$ (nm)
300	50	28	20	5
600	49	30	18	4
900	36	19	21	2

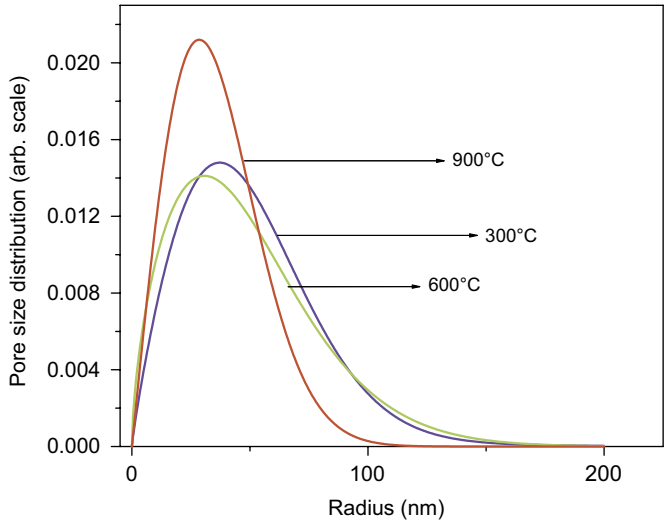

Fig. 6. The type-1 (larger size) pore size distribution of the NiO powder samples.

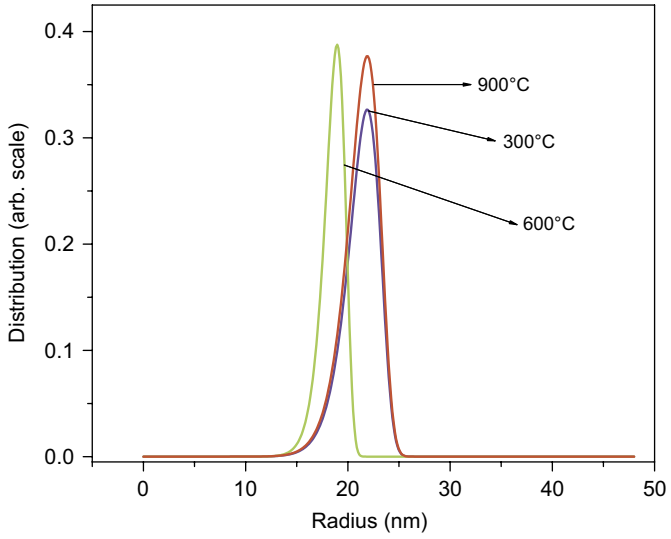

Fig. 7. The type-2 (smaller size) length scale pore size distribution of the NiO powder samples.

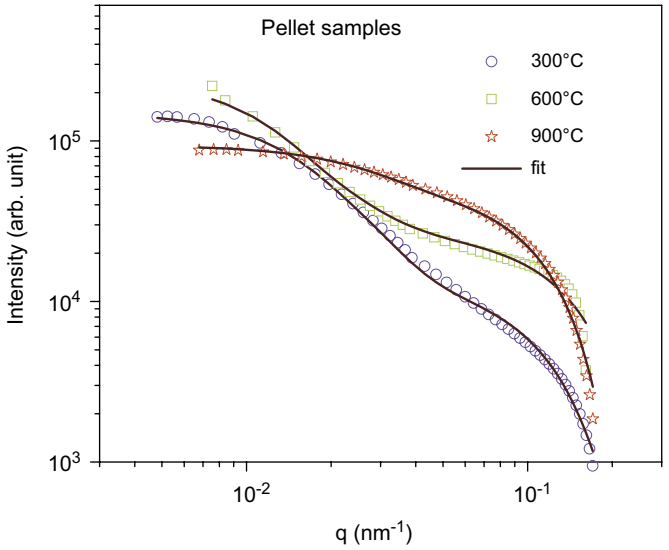

Fig. 8. SANS profiles of pelleted samples with different heat treatment temperatures.

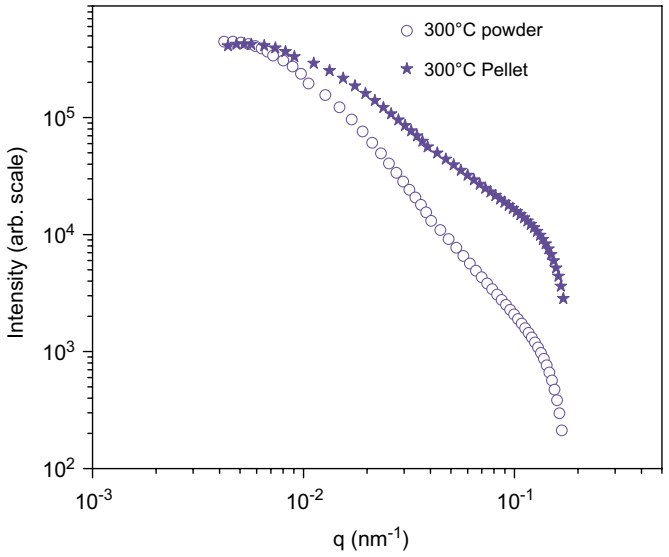

Fig. 9. SANS profile for the powder (pd-300) and pellet (pl-300) samples is compared.

pd-600, and pd-900 are depicted in Fig. 7. From the figure it is discernible that the distribution for the type-2 pores lies in the significantly lower length scale than that for the type-1 pores and is much less polydisperse in nature compared to the type-1 pores. It is observed from Fig. 7 that on an average there has not been significant modifications of the type-2 pores due to heat treatment, although from a close look it appears that for the 600 °C sample the distribution shifts slightly towards lower radius. However, it is not easy to comment on this slight variation vis-à vis some additional effect which may occur at 600 °C, because the length scale of the smaller distribution lies almost at the high q resolution limit of the measurements. At this point, it is worth mentioning that the mesoscopic structure as observed from the SEM micrograph is quite complicated and with some level of hierarchy, and hence the analysis of the density fluctuation from SANS data is not an easy task on a quantitative level. However, the situation can be handled with introduction of a relatively simpler model as described above, particularly when the aim is mainly to estimate the pore size distribution only.

As mentioned earlier SANS experiments have also been carried out on the pellet samples (pressure ~150 Mpa). Care has been taken to keep the palletizing condition identical for all the three samples. SANS data for the pelleted samples are plotted in Fig. 8. It is evident from the figure that in this case also the presence of the two length scales exists and the structure is significantly altered with heat treatments. However, the pore structure at particular temperature with and without pelletization differs significantly. This has been emphasized in Fig. 9 by comparing

Table 2
Parameters of the pore size distributions for pellet samples

Sample (°C)	$\langle r_{larger} \rangle$ (nm)	$[\langle r^2_{larger} \rangle - \langle r_{larger} \rangle^2]^{0.5}$ (nm)	$\langle r_{smaller} \rangle$ (nm)	$[\langle r^2_{smaller} \rangle - \langle r_{smaller} \rangle^2]^{0.5}$ (nm)
300	42	25	16	4
600	30	23	15	4
900	29	19	20	2

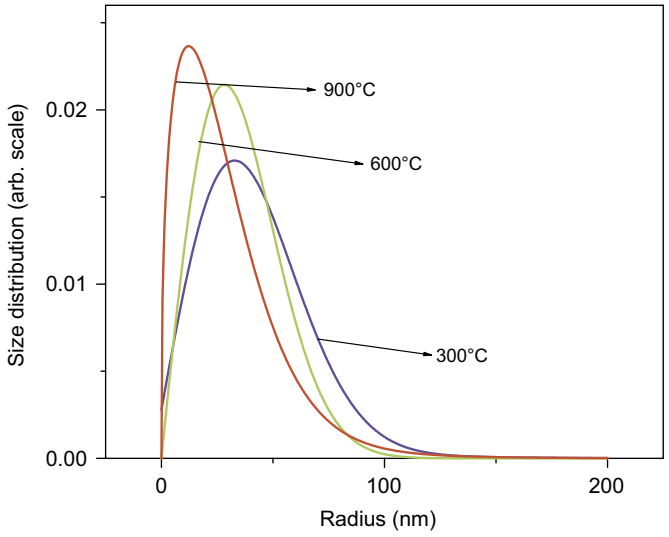

Fig. 10. Type-1 (larger size) pore size distribution in pelleted samples with different heat treatment temperatures.

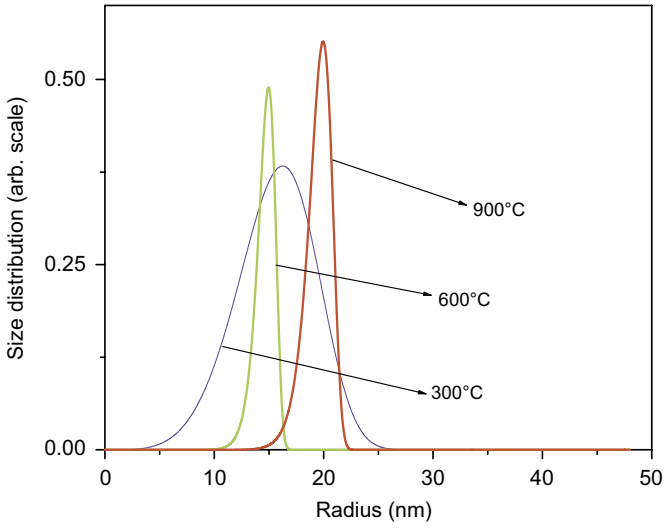

Fig. 11. Type-2 (smaller size) pore size distribution in pellet samples at different heat treatment temperatures.

the profiles of both powder and pellet samples for 300 °C temperature. It is clearly seen that the profile becomes broader in case of the pelleted sample as compared to powder sample as expected. Due to mechanical pressure during the palletizing, the type-1 pores shrink quite significantly which leads to the broadening of the SANS profiles. However, in this case also the qualitative features of the profile remain unmodified, i.e., the existence of the pores in the two length scale remains, although the size of the type-1 pores is reduced. The important parameters for the pelleted samples obtained from the fitting are tabulated in Table 2. The type-1 pore size distributions for the pelleted samples are shown in Fig. 10. It is interesting to observe from Figs. 6 and 10 that the broadening and the high-end tail are significantly reduced in this case compared to the un-pelleted samples. However, the type-2 pores (finer pores) (Fig. 11) have been found almost unmodified under compaction pressure. This is due to the fact that the applied pressure does not alter much the agglomeration in the smaller length scales.

At this juncture it is interesting to discuss the scaling of scattering function under heat treatment. In fact the idea of scaling phenomenon, initially implemented mostly in a dynamical approach to alloys and other complex systems [30–32], it deals with the fact that a characteristic length (L_c) may be defined for an evolving system and then a normalized structure factor $F(q, L_c)$ can be constructed in such a way that $F(q,L_c)$ at various evolution steps are independent of evolution parameters:

$$F(q, L_c) = \frac{[L_c]^{-3} I(q)}{\sum_i q_i^2 I(q_i) \delta q_i}, \tag{7}$$

where δq_i is experimental q increment. When the scaling is validated the $F(q,L_c)$ at various evolution steps overlaps one over another. However, the absence of the scaling is indicated by the deviation from the overlapping of the normalized structure factor. In most of the previous studies inverse of the first moment of q has been taken as the measure of the L_c:

$$q_1 = \frac{\sum_i I(q_i) q_i \mathrm{d}q_i}{\sum_i I(q_i) \mathrm{d}q_i}, \tag{8}$$

where summation limits have been taken same as experimental q range. However, sometimes the average radius or the radius of gyration has also been employed [31]. It is interesting to note that in the present case q_1^{-1}, as a sole characteristic length for the whole profile, does not lead to the scaling of the structures at different heat treatment temperatures. As in the present case there exist two length scales it provoked us to verify the scaling of the profiles using two characteristic length scales corresponding to the two regions of the profiles (one in the q range from 0.003 to 0.04 nm^{-1} and the other from 0.04 to 0.17 nm^{-1}). The normalized structure factors for the powder are depicted in

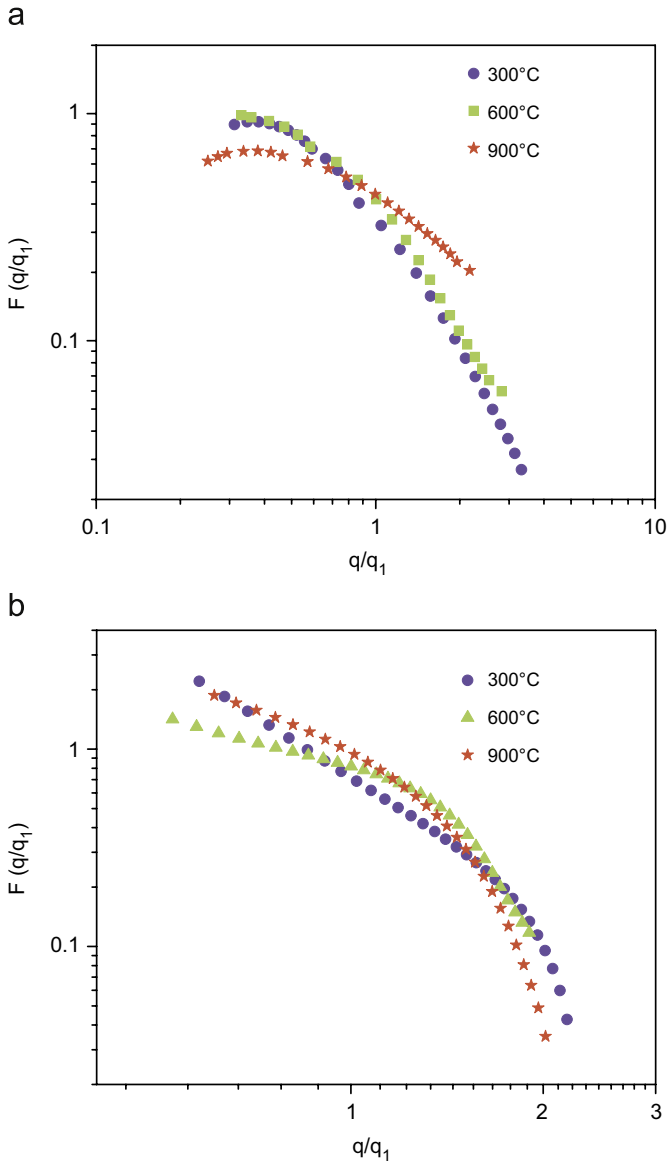

Fig. 12. (a) Scaled structure factors are plotted with q/q_1, for powder samples with different heat treatment temperatures in q range 0.003–0.04 nm^{-1}. (b) Scaled structure factors are plotted with q/q_1, for powder samples with different heat treatment temperatures in q range 0.04–0.17 nm^{-1}.

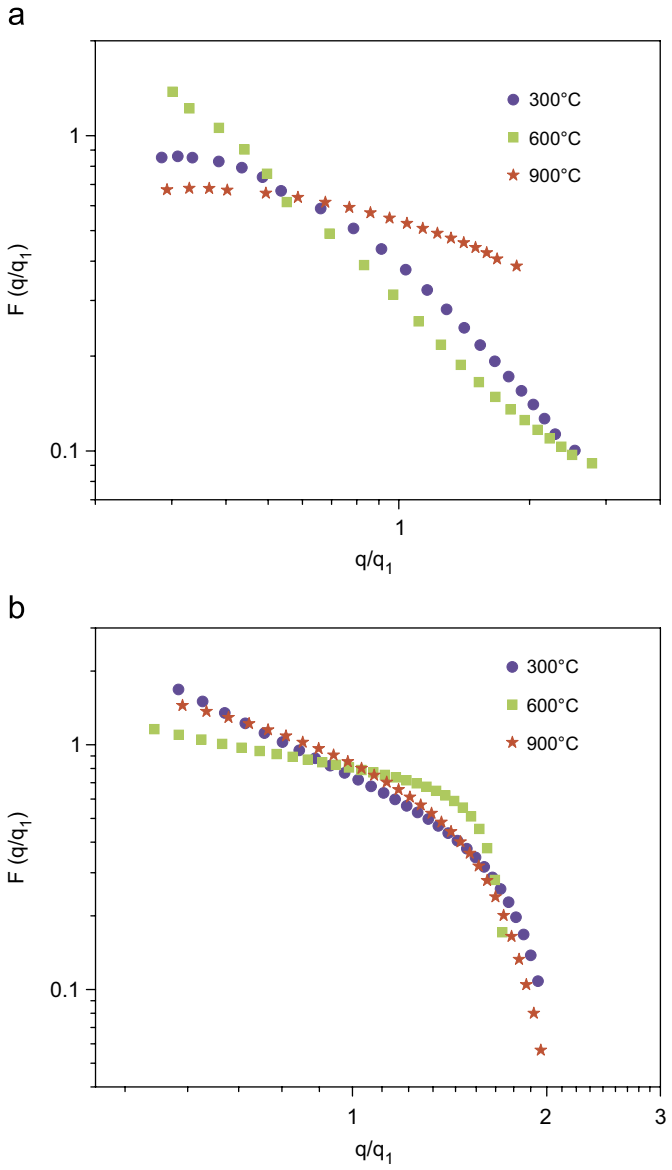

Fig. 13. (a) Scaled structure factors are plotted with q/q_1, for pelleted samples at different heat treatment temperatures in q range 0.003–0.04 nm^{-1}. (b) Scaled structure factors are plotted with q/q_1, for pelleted samples at different heat treatment temperatures in q range 0.04–0.17 nm^{-1}.

Figs. 12a and b. The same for pellet samples are depicted in Figs. 13a and b. From these figures it is evident that even with employing two characteristic length scales for two regions, the scaling has not been observed for both the powder and the pelleted samples. This may be attributed to the following. In crystalline solids the primary densification mechanism is grain boundary diffusion. The surface diffusion, non-densification mechanism, does not affect the densification, but change the surface topology. If this diffusion process is isotropic during the heat treatment, it is expected that the scaling should hold for the structure factors. However, grain boundary diffusion [33] leads to the deviation from the isotropic diffusion. It is important to note that the earlier simulation studies on the heat treatment behavior of the amorphous nano-clusters and nano-crystals [33] show that the neck formation is asymmetric for nano-crystals. The absence of the scaling of the normalized structure factor in the present case has been attributed to the above phenomenon, i.e., the anisotropic/asymmetric diffusion process.

4. Conclusions

The XRD measurement showed the crystallinity of the NiO powder with average crystallite size of ~9 nm. DLS and the SEM of the virgin powder revealed the average agglomerate size to be ~1 μm. Existence of pore structures at two widely separated length scales in the agglomerates

was elucidated from SANS. It has been shown that the larger pore size has been significantly modified under heat treatment and also by palletizing. Shrinkage of the pores occurs with increasing heat treatment temperature and is attributed to mass transport by grain boundary diffusion. Due to the diffusion driven mass transport, pore structures evolve asymmetrically with heat treatment temperature, which is revealed from the absence of scaling of the normalized structure factors even with the introduction of two different characteristic lengths for zone-1 and zone-2.

Appendix A. Some essential aspects of multiple scattering

At this juncture it is worthy to mention that Eqs. (2), (3), and (6) demand the criteria of single scattering approximation (SSA) to be fulfilled [34–36]. In such a case the probing radiation, while passing the specimen, is either scattered only once from a single particle or not at all. For the situation where SSA holds good the functionality or shape of the scattering profile remains invariant with respect to sample thickness or wavelength of the probing radiation. In other words, the scattering profiles, recorded with variation of sample thickness or wavelength, are different as regards to a scale factor only. The profiles are then indistinguishable from each other after suitable normalization or if presented in the absolute intensity scale. However, for samples with significant scattering contrast, large inhomogeneity size, etc., multiple scattering comes into picture when sample thickness is significantly larger than scattering mean free path. The strength of multiple scattering can be determined by performing SANS experiments for samples with different thickness values or using different wavelength of the probing radiation. The signature of multiple scattering is the functional dependence of measured profiles on the sample thickness or the wavelength of the probing radiation. The effect of multiple scattering and the data analysis procedure depend upon the degree of multiple scattering, which can be conveniently measured by N, the ratio of the sample thickness t to SMFP (L). N is a statistical number signifying the average number of scattering interaction radiation has undergone while passing through the sample. It is related to absolute scattering cross-section by the following relation:

$$\int \mathrm{d}\Omega \frac{\mathrm{d}\Sigma(q)}{\mathrm{d}\Omega} = \frac{1-\exp(-N)}{t},$$

where t is sample thickness, for very thin sample

$$\int \mathrm{d}\Omega \frac{\mathrm{d}\Sigma(q)}{\mathrm{d}\Omega} \approx L^{-1},$$

and under small-angle approximation,

$$\int \mathrm{d}qq \frac{\mathrm{d}\Sigma(q)}{\mathrm{d}\Omega} \approx L^{-1}\lambda^{-2}.$$

In the diffraction limit $L \approx \lambda^{-2}$ and hence, for very thin samples $\mathrm{d}\Sigma/\mathrm{d}\Omega(q)$ is independent of t and λ. We have simulated the optimum effect of the multiple scattering for the present experiment and with sample thickness ~1 mm. Scattering mean free path for spherical system is given by

$$L = \frac{2\langle R^3\rangle}{3\phi\langle R^4\lambda^2 D^2\rangle},$$

where ϕ is porosity, λ is the wavelength of the probing radiation, and D is the difference of scattering length density between matrix and pores. $\langle R^3\rangle$ and $\langle R^4\rangle$ denote third and fourth moment of pore radius (R). The nth moment of pore radius can be defined as

$$\langle R^n\rangle = \frac{\int R^n D(R)\,\mathrm{d}R}{\int D(R)\,\mathrm{d}R}.$$

From the above formula L was estimated to be nearly 1 mm for a porosity value of 0.1 and λ of 0.31 nm. So the value of N becomes ~1 for the present case. A single scattering profile has been simulated for an ensemble of spherical scatterers following the Wiebull distribution with average radius ~80 nm. SANS profiles in the present case correspond to lower average radius, and hence smaller multiple scattering effect. The simulated profile for $N=1$ and the single scattering profile are plotted in Fig. 14. From the figure it is evident that the functionality of the profile with $N=1$ is slightly broader at very low q region although the high q region remains almost unaffected. However, as the framework of the present work does not cope with the detail elaboration of the effect of multiple scattering, the same has not been dealt with for the present case. Rather the present work concentrates on the materials aspect of the sintering behavior and the evolution of the pore structure. Due to the limitation of neutron flux at the sample position, we restricted our experiments for minimum sample thickness ~1 mm. It has been found that lowering the sample thickness reduces the quality of the signal; however, no significant modifications of the profile was observed within the statistical fluctuations in the q

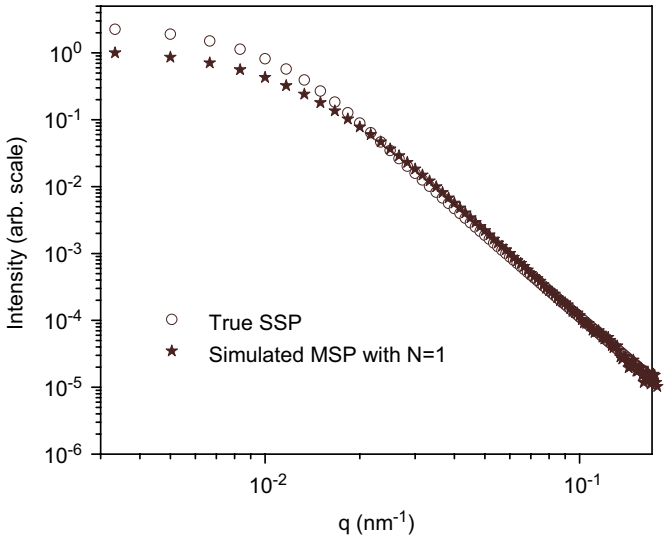

Fig. 14. The simulated multiple scattering profile with $N=1$ is compared to the corresponding single scattering profile.

range beyond $0.02\,nm^{-1}$ as is also the case from the simulated data in Fig. 14. That is why the thickness of the all samples was kept $\sim$1 mm.

References

[1] C.B. Murray, C.R. Kagan, M.G. Bawendi, Annu. Rev. Matter Sci. 30 (2006) 545.
[2] G.-M. Chow, N. Ivanova Noskova, Nano-structured Materials Science and Technology, Kluwer Academic publishers, Dordrecht, 1998.
[3] L. Mazzola, Nat. Biotechnol. 21 (2003) 1137.
[4] R. Paul, J. Wolfe, P. Hebert, M. Sinkula, Nat. Biotechnol. 20 (2003) 277.
[5] R.W. Siegel, in: F.E. Fujita (Ed.), Physics of New Materials, Springer, Heidelberg, 1994, p. 65.
[6] J. Karch, R. Birringer, H. Gleiter, Nature (London) 330 (1987) 556.
[7] I.-W. Chen, X.-H. Wang, Nature 404 (2000) 168.
[8] P.K. Krishnankutty-Nair, K. Keizer, A.J. Burggraaf, T. Okubo, H. Nagamoto, S. Morooka, Nature 358 (1992) 48.
[9] B. Pejova, T. Kocareva, M. Najdoski, I. Grzdanov, Appl. Surf. Sci. 165 (2000) 271.
[10] H. Sato, T. Minami, S. Takata, T. Yamada, Thin Solid Films 236 (1993) 27.
[11] K. Liu, M. Anderson, J. Electrochem. Soc. 143 (1996) 124.
[12] V. Srinivasan, J. Weidner, J. Electrochem. Soc. 144 (1997) L210.
[13] J. He, H. Lindström, A. Hagfeldt, S.-E. Lindquist, J. Phys. Chem. B103 (1999) 8940.
[14] W.D. Kingery, H.K. Bowden, D.R. Uhlmann, in: Wiley Series on the Science and Technology of the Materials, second ed., Wiley, New York, 1976, p. 1032.
[15] D. Vollath, D.V. Szabo, Nanostruct. Mater. 4 (1994) 927.
[16] U. Keiderling, A. Moller, A. Wiedenmann, M. Winterer, H. Hahn, Physica B 874 (2000) 276.
[17] U. Keiderling, A. Wiedenmann, V. Srdic, M. Winterer, H. Hahn, J. Appl. Crystallogr. 33 (2000) 483.
[18] A. Guinier, G. Fournet, B.C. Walker, L.K. Yudowith, Small Angle Scattering of X-rays, Wiley, New York, 1955, pp. 167–195.
[19] A.K. Patra, J. Bahadur, S. Mazumder, S. Nair, R.D. Purohit, A.K. Tyagi, J. Nanosci. Nanotechnol. 8 (2007) 1–6.
[20] S. Mazumder, D. Sen, T. Sarvanan, P.R. Vijayraghavan, J. Neutron Res. 9 (2001) 39.
[21] P.W. Schmidt, R. Height, Acta Crystallogr. 13 (1960) 480.
[22] J.A. Lake, J. Appl. Cryst. 23 (1967) 191.
[23] P.J. McMahon, S.D. Moss, J. Appl. Cryst. 32 (1999) 956.
[24] S. Mazumder, D. Sen, S.K. Roy, M. Hainbuchner, M. Baron, H. Rauch, J. Phys. Condens. Matter 13 (2001) 5089.
[25] D. Sen, A.K. Patra, S. Mazumder, S. Ramanathan, J. Alloys Compds. 340 (2002) 236.
[26] D. Sen, T. Mahata, A.K. Patra, S. Mazumder, B.P. Sharma, J. Phys. Condens. Matter 16 (2004) 6229.
[27] D. Sen, A.K. Patra, S. Mazumder, S. Ramanathan, J. Alloys Compds. 361 (2003) 270.
[28] P.W. Schmidt, J. Appl. Cryst. 15 (1982) 567.
[29] W. Weibull, J. Appl. Mech. 18 (3) (1951) 293–297.
[30] S. Mazumder, D. Sen, I.S. Batra, R. Tewari, G.K. Dey, S. Banerjee, A. Sequeira, H. Amentisch, S. Bernstorff, Phys. Rev. B 60 (1999) 822.
[31] S. Mazumder, D. Sen, A.K. Patra, S.A. Khadilkar, R.M. Cursetji, R. Loidl, M. Baron, H. Rauch, Phys. Rev. Lett. 93 (2004) 255704.
[32] S. Mazumder, D. Sen, A.K. Patra, S.A. Khadilkar, R.M. Cursetji, R. Loidl, M. Baron, H. Rauch, Phys. Rev. B 72 (2005) 224208.
[33] K. Tsuruta, A. Omeltchenko, R.K. Kalia, P. Vashishta, Europhys. Lett. 33 (6) (1996) 441.
[34] S. Mazumder, A. Sequeira, Pramana J. Phys. 38 (1992) 95.
[35] S. Mazumder, A. Sequeira, Phys. Rev. B 39 (1989) 6370.
[36] S. Mazumder, A. Sequeira, Phys. Rev. B 41 (1990) 6272.